# Supplementary material for "A SAW-driven modular acoustofluidic tweezer"

Dachuan Sang,[a] Suyu Ding,[a] Qinran Wei,[a] Fengmeng Teng,[b] Haixiang Zheng,[a] Yu Zhang,[a] Dong Zhang,[a*‡] and Xiasheng Guo[a*‡]

## S1. Lamb wave excitation in the QG plate

As illustrated in Fig. S2, the displacement field in the QG plate can be written as $(\nabla\varphi + \nabla\times\boldsymbol{\psi})$, where $\varphi$ and $\boldsymbol{\psi}$ are the potentials for longitudinal and transverse waves, respectively. The potentials satisfy the following wave equations (for time-harmonic excitation),

$$\frac{\partial^2\varphi}{\partial x^2}+\frac{\partial^2\varphi}{\partial z^2}+{k_{\mathrm{L}}}^2\varphi=0, \tag{S1}$$

$$\frac{\partial^2\psi}{\partial x^2}+\frac{\partial^2\psi}{\partial z^2}+{k_{\mathrm{T}}}^2\psi=0, \tag{S2}$$

where $k_{\mathrm{L}}=\omega\sqrt{\rho/(\lambda+2\mu)}$ and $k_{\mathrm{T}}=\omega\sqrt{\rho/\mu}$, $\lambda$ and $\mu$ are Lamé constants, $\rho$ is the density of QG. Considering the $y$-independence of the displacement field, $\boldsymbol{\psi}$ only has non-zero components along the $y$-direction, which is simply written as $\psi$.

The displacement along the $x$-axis ($U$), the $z$-axis ($W$), and the corresponding stress components can be represented in terms of $\varphi$ and $\psi$,[1]

$$U=\frac{\partial\varphi}{\partial x}-\frac{\partial\psi}{\partial z}, \tag{S3}$$

$$W=\frac{\partial\varphi}{\partial z}+\frac{\partial\psi}{\partial x}, \tag{S4}$$

$$\sigma_{zz}=\lambda\left(\frac{\partial U}{\partial x}+\frac{\partial W}{\partial z}\right)+2\mu\frac{\partial W}{\partial z}=\lambda\left(\frac{\partial^2\varphi}{\partial x^2}+\frac{\partial^2\varphi}{\partial z^2}\right)+2\mu\left(\frac{\partial^2\varphi}{\partial z^2}+\frac{\partial^2\psi}{\partial x\partial z}\right), \tag{S5}$$

$$\sigma_{xz}=\mu\left(\frac{\partial U}{\partial z}+\frac{\partial W}{\partial x}\right)=\mu\left(2\frac{\partial^2\varphi}{\partial x\partial z}+\frac{\partial^2\psi}{\partial x^2}-\frac{\partial^2\psi}{\partial z^2}\right). \tag{S6}$$

The upper surface of the plate (at $z=h$) is confined by

$$\sigma_{zz}=\begin{cases}\sigma_0 e^{\mathrm{i}(k_0x-\omega t)} & \text{for } |x|\le b,\\ 0 & \text{for } |x|>b,\end{cases} \tag{S7}$$

$$\sigma_{xz}=0, \tag{S8}$$

where the wave number $k_0$ satisfies

$$k_0=k_{\mathrm{coup}}\sin\theta_{\mathrm{R1}}=\frac{2\pi f}{c_{\mathrm{coup}}}\sin\theta_{\mathrm{R1}}=\frac{2\pi f}{c_{\mathrm{coup}}}\frac{c_{\mathrm{coup}}}{c_{\mathrm{SAW}}}=\frac{2\pi f}{c_{\mathrm{SAW}}}. \tag{S9}$$

Here, $k_{\mathrm{coup}}$ is the wave number in the couplant, with $\sigma_0$ being the stress amplitude at $z=h$.

[a] *Address: Key Laboratory of Modern Acoustics (MOE), School of Physics, Collaborative Innovation Centre of Advanced Microstructures, Nanjing University, Nanjing 210093, China.*
[b] *Address: Department of Clinical Laboratory, Jiangsu Provincial Hospital of Traditional Chinese Medicine, Nanjing 210029, China.*
*E-mail: guoxs@nju.edu.cn, dzhang@nju.edu.cn
‡ Dr. Dong Zhang and Dr. Xiasheng Guo are Fellows at the Collaborative Innovation Center for Cardiovascular Disease Translational Medicine, Nanjing Medical University..

The lower surface ($z = -h$) is confined by

$$\sigma_{zz} = 0,\ \sigma_{xz} = 0. \tag{S10}$$

Then, $\varphi$ and $\psi$ can be represented using Fourier integrals, separating them into symmetric and asymmetric parts,

$$\varphi = \varphi_{\mathrm{s}} + \varphi_{\mathrm{a}} = \int_{-\infty}^{\infty} A(k)\cos(pz)\mathrm{e}^{\mathrm{i}kx}\mathrm{d}k + \int_{-\infty}^{\infty} B(k)\sin(pz)\mathrm{e}^{\mathrm{i}kx}\mathrm{d}k, \tag{S11}$$

$$\psi = \psi_{\mathrm{s}} + \psi_{\mathrm{a}} = \int_{-\infty}^{\infty} C(k)\cos(qz)\mathrm{e}^{\mathrm{i}kx}\mathrm{d}k + \int_{-\infty}^{\infty} D(k)\sin(qz)\mathrm{e}^{\mathrm{i}kx}\mathrm{d}k, \tag{S12}$$

where $A(k)$, $B(k)$, $C(k)$ and $D(k)$ can be determined by boundary conditions. The time-harmonic factor $\mathrm{e}^{-\mathrm{i}\omega t}$ is omitted here.

Based on the boundary conditions, the $z$ component displacement is

$$\begin{aligned} W = \frac{\sigma_0}{2\pi\mu}\int_{-\infty}^{\infty} p \Bigg[ &-\frac{(k^2-q^2)\sin(qh)\sin(pz) - 2k^2\sin(ph)\sin(qz)}{\Delta_{\mathrm{s}}} \\ &+ \frac{(k^2-q^2)\cos(qh)\cos(pz) - 2k^2\cos(ph)\cos(qz)}{\Delta_{\mathrm{a}}}\Bigg]\frac{\sin[(k_0-k)b]}{k_0-k}\mathrm{e}^{\mathrm{i}kx}\mathrm{d}k, \end{aligned} \tag{S13}$$

in which

$$\Delta_{\mathrm{s}} = (k^2-q^2)^2\cos(ph)\sin(qh) + 4k^2pq\cos(qh)\sin(ph), \tag{S14}$$

$$\Delta_{\mathrm{a}} = (k^2-q^2)^2\cos(qh)\sin(ph) + 4k^2pq\cos(ph)\sin(qh). \tag{S15}$$

The integrals can be calculated in the complex plane of $k$ with the help of the well-known Residue theorem. Then, the $z$ component displacement at the upper surface ($z = h$) can be obtained as

$$W_0 = \frac{\mathrm{i}\sigma_0}{\mu}\left[\sum_{k_{\mathrm{s}}}\frac{\sin[(k_0-k)b]}{k_0-k}\cdot\frac{p(q^2+k^2)\sin(qh)\sin(ph)}{\Delta_{\mathrm{s}}{}'} - \sum_{k_{\mathrm{a}}}\frac{\sin[(k_0-k)b]}{k_0-k}\cdot\frac{p(q^2+k^2)\cos(ph)\cos(qh)}{\Delta_{\mathrm{a}}{}'}\right]\mathrm{e}^{\mathrm{i}kx}, \tag{S16}$$

where $\Delta_{\mathrm{s}}{}'$ and $\Delta_{\mathrm{a}}{}'$ are the derivatives of $\Delta_{\mathrm{s}}$ and $\Delta_{\mathrm{a}}$ with respect to $k$. $\sum_{k_{\mathrm{s}}}$ and $\sum_{k_{\mathrm{a}}}$ are summations over all wave numbers of symmetric and asymmetric modes existing in the QG plate. The possible wave numbers can be determined from the dispersion curves for the given frequency-thickness product $f\cdot d$.

In acoustofluidic applications, the out-of-plane displacement (i.e. $W_0$) is the dominant component that leaks into the fluid. In the $W_0$ expression, the excitability of each mode can be seen as a product of some terms. Notably, the term $\sin[(k_0-k)b]/(k_0-k)$ is a Sinc function depend on $(k_0-k)$, with the principle maximum obtained at $k = k_0$, giving $c_{\mathrm{p}} = c_{\mathrm{SAW}}$. Therefore, among the Lamb modes excited in MAFT, the one with the phase velocity closest to the SAW speed ($c_{\mathrm{SAW}}$) behaves as the dominant mode. In other words, the generated Lamb waves tend to propagate at a speed that matches $c_{\mathrm{SAW}}$.

## S2. Methods for FE simulation and material parameters

2D simulations of the acoustic fields were conducted in the "Frequency Domain" study in the FE software COMSOL Multiphysics. Solid displacements in the LN domain were solved with the "Solid Mechanics-Piezoelectric Material" and the "Electrostatics-Charge Conservation, Piezoelectric" interfaces. The excitation voltage was introduced by applying the "Electric Potential" boundary condition in the region covered by the IDTs. "Perfect Matching Layers" were employed to minimize the reflection of waves at the boundaries. The displacements in the QG plates were solved with the "Solid Mechanics" interface.

The "Pressure Acoustics, Frequency Domain" interface was employed to calculate the acoustic fields in the PDMS domain. For the fluid (water) and couplant (silicone oil), the acoustic fields were calculated via the "Thermoviscous Acoustics, Frequency Domain" interface. The "Acoustic-Thermoviscous Acoustic Boundary" was adopted to describe the fluid/PDMS coupling, and the PDMS/QG coupling described with the "Acoustic-Structure Boundary". The "Thermoviscous-Acoustics-Structure Boundary" was employed to model the couplings at the fluid/QG, couplant/QG and couplant/LN

**Table S1** List of material parameters used in simulations

| Material | Parameter | Value |
|---|---|---|
| Water [2] | Density | 998 kg m$^{-3}$ |
| | Longitudinal wave speed | 1495 m s$^{-1}$ |
| | Dynamic viscosity | 0.893 mPa s |
| | Bulk viscosity | 2.47 mPa s |
| | Specific heat capacity | 4183 J kg$^{-1}$ K$^{-1}$ |
| | Thermal conductivity | 0.603 W m$^{-1}$ K$^{-1}$ |
| | Thermal expansion coefficient | $2.97 \times 10^{-4}$ K$^{-1}$ |
| | Specific heat capacity ratio | 1.014 |
| Polydimethylsiloxane (PDMS) [3] | Density | 1070 kg m$^{-3}$ |
| | Longitudinal wave speed | 1030 m s$^{-1}$ |
| | Absorption coefficient | 84.8 dB cm$^{-1}$ |
| Quartz glass [a] | Density | 2203 kg m$^{-3}$ |
| | Young's modulus | $7.5 \times 10^{10}$ Pa |
| | Poisson ratio | 0.17 |
| 128° $Y$-cut $LiNbO_3$ [b] | Density | 4700 kg m$^{-3}$ |
| | Elastic matrix | See table note |
| | Dielectric matrix | See table note |
| | Piezoelectric matrix | See table note |
| Silicone oil (5 cSt) [4,5] | Density | 974 kg m$^{-3}$ |
| | Longitudinal wave speed | 1004 m s$^{-1}$ |
| | Dynamic viscosity | 4.565 mPa s |
| | Bulk viscosity | 67.2 mPa s |
| | Specific heat capacity | 1460 J kg$^{-1}$ K$^{-1}$ |
| | Thermal conductivity | 0.15 W m$^{-1}$ K$^{-1}$ |
| | Thermal expansion coefficient | $9.2 \times 10^{-4}$ K$^{-1}$ |
| | Specific heat capacity ratio | 1.174 |

[a] Parameters adopted from supplier's data sheet. [b] Parameters adopted from the material library in COMSOL.

interfaces. The ceilings of the PDMS channels were considered as "Impedance" boundaries.

The acoustic streaming inside the droplet was calculated in "Stationary" studies via the "Laminar Flow" interface and the "Acoustic Streaming Domain Coupling" condition. The droplet surface was constrained using the "Stationary Free Surface" condition in the "Laminar Flow" interface.

The material parameters used in the simulation are shown in Table S1. In order to reduce the computational effort, the widths of the LN and QG plates were reduced in FE models. All simulations were performed at an excitation voltage of $V_{\mathrm{p-p}} = 10$ V. The results of the Type-420 IDT module/0.3 mm-thickness QG (with PDMS micro-chamber) and Type-200 IDT module/0.17 mm-QG (with sessile droplet) are shown in Fig. S3(a) and (b). At the driving frequency $f = 9.5$ MHz, the acoustic field in the QG, PDMS and microfluidic domains are shown in Fig. S3(a), where the green arrows indicate the ARF field acting on Rayleigh particles with $\Phi > 0$. Figure S3(b) shows the results of the acoustic field in the QG at the excitation of $f = 19.9$ MHz, along with the magnitude of the acoustic streaming in the sessile droplet and the streamlines.

## S3. Consistency of performance

Consistency experiments were performed for the configuration that two Type-300 IDT modules are coupled with a 0.3 mm-thickness QG plate to generate standing Lamb waves in the latter. The surface displacements of the QG plate were measured with a laser vibrometer at the excitation frequency of $f = 13.05$ MHz and voltage $V_{\mathrm{p-p}} = 30$ mV (corresponding to a power of 23.50 dBm) for five repeated experiments. The coupling between the IDT module and the QG plate is redone in each repeat. The measured average amplitudes at the field antinodes are shown in Fig. S8. As the average amplitudes were all close to 1.5 nm, the consistency of MAFT performance is demonstrated.

## S4. Supplementary videos

Video S1: The assembly of MAFT.
Video S2: Particle patterning with MAFT.
Video S3: Patterning of MCFs cells with MAFT.

Video S4: Particle manipulation with MAFT.
Video S5: Separation of HL-60 cells/RBCs with MAFT.
Video S6: Concentration of PS particles with MAFT.
Video S7: Concentration of HUVECs with MAFT.

## Supplementary Figures

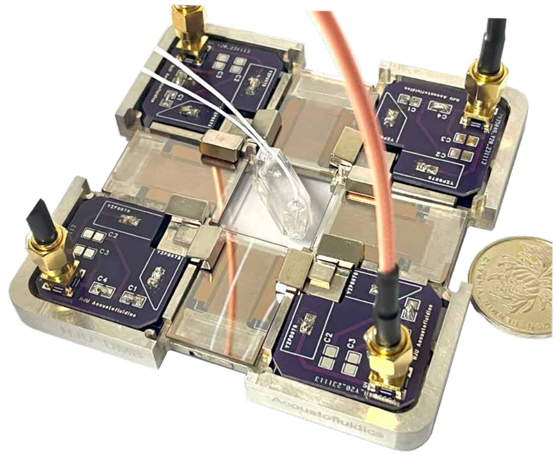

**Fig. S1** The photograph of an assembled MAFT.

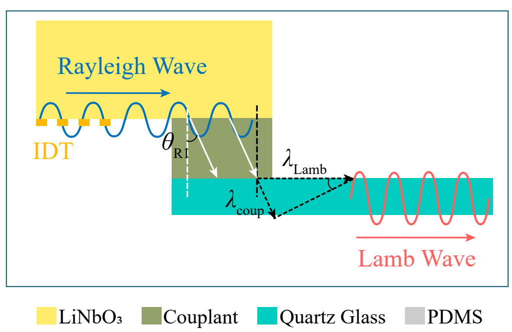


**Fig. S2** Illustration of the Lamb wave excitation in the QG plate.

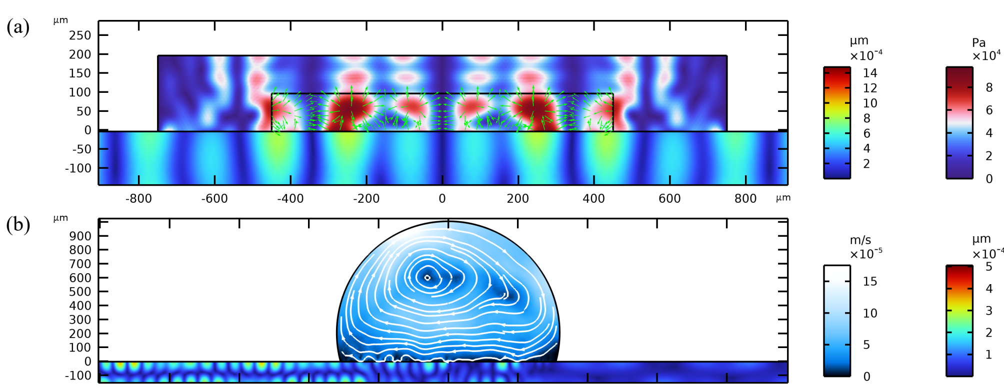


**Fig. S3** Simulation results for two configurations. (a) Two Type-420 IDT modules and excites standing Lamb waves in a PDMS micro-chamber fabricated on a $0.3$ mm thick QG plate. (b) A Type-200 IDT module excites streaming in a sessile droplet placed on a $0.17$ mm thick QG plate.

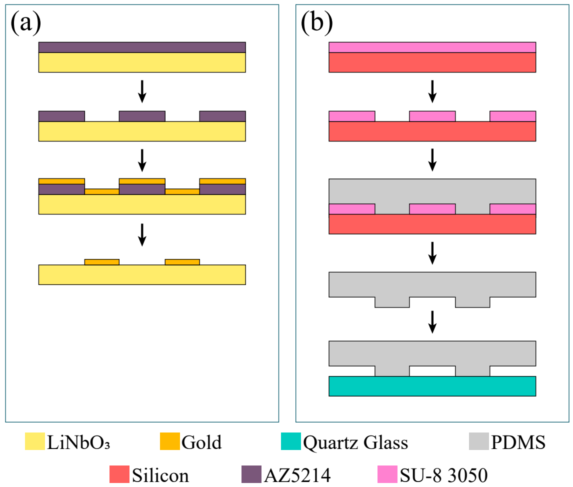


**Fig. S4** Fabrication process of the IDT modules and Type-chamber/Type-channel function modules. (a) The fabrication of an IDT module includes steps of spin-coating (of AZ5214 photoresist), UV lithography, magnetron sputtering, and lift-off. (b) The fabrication of Type-chamber/Type-channel function modules include spin-coating (of SU-8 300 photoresist), UV lithography, PDMS molding, and PDMS/QG bonding.

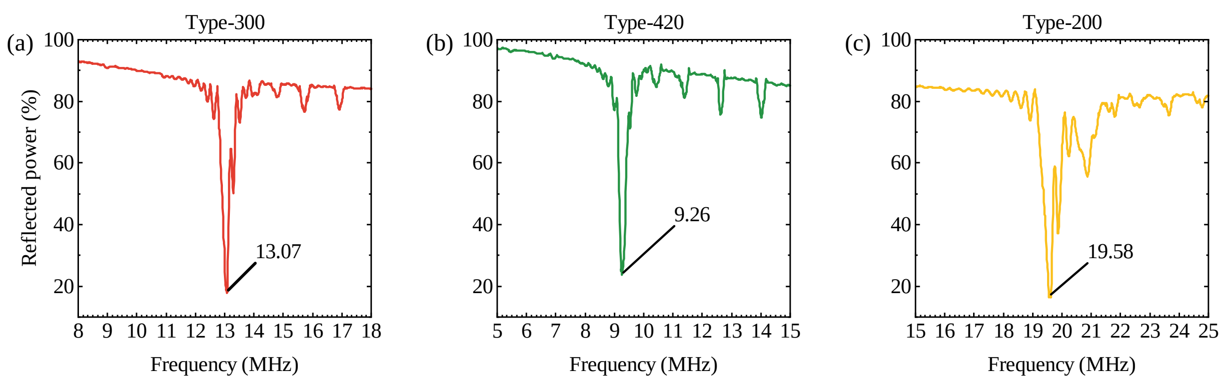


**Fig. S5** The network parameter S11 as a function of the driving frequency for three IDT modules. (a), (b), and (c) correspond to the Type-300, Type-420, and Type-200 IDT modules, respectively. The frequencies exhibiting the lowest reflections are at 13.07 MHz, 9.25 MHz, and 19.58 MHz, respectively.

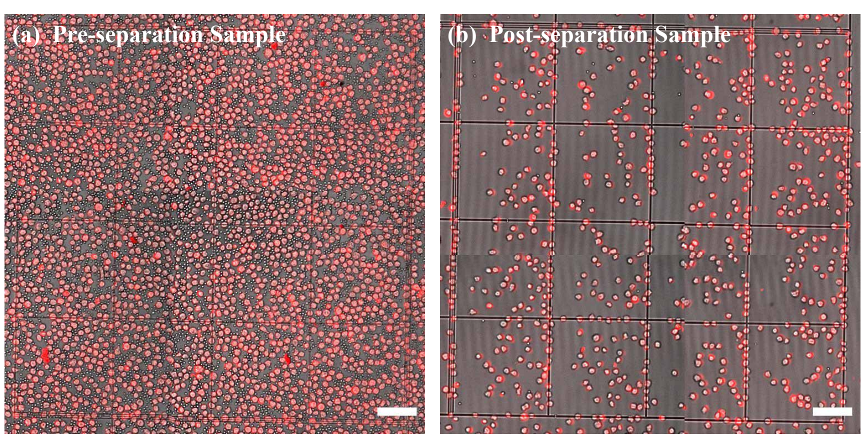


**Fig. S6** Images of the pre- and post-separation samples. (a) The initial mixed cell sample (HL-60/RBCs), (b) the separated HL-60 cell fraction. Fluorescently labeled HL-60 cells (red) are superimposed on bright-field images. Scale bars: 100 µm.

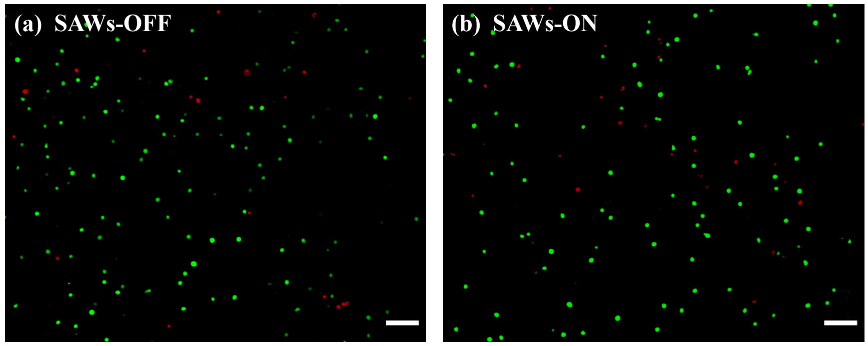


**Fig. S7** Examination of cell viability after separation. (a) SAWs-OFF and (b) SAWs-ON groups showing live (green, calcein-AM) and dead (red, PI) HL-60 cells. Scale bars: $100\ \mu m$.

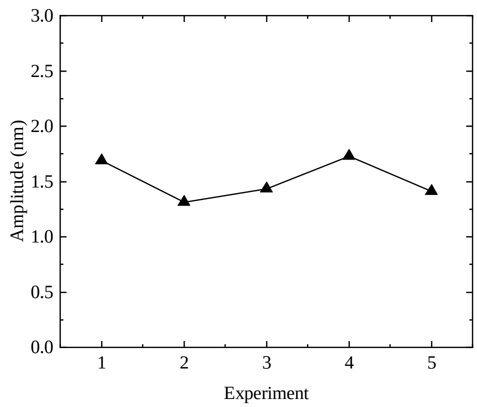


**Fig. S8** The average amplitude at the standing Lamb wave field antinodes measured in five repeated experiments where two Type-300 IDT modules are coupled to a $300\ \mu m$-thickness QG plate. The coupling between the IDT modules and the QG plate are redone before each repeat.

## References


1 I. A. Viktorov, *Rayleigh and Lamb Waves: Physical Theory and Applications*, Springer US, 2013.

2 P. B. Muller, R. Barnkob, M. J. H. Jensen and H. Bruus, *Lab Chip*, 2012, **12**, 4617.

3 Z. Ni, C. Yin, G. Xu, L. Xie, J. Huang, S. Liu, J. Tu, X. Guo and D. Zhang, *Lab Chip*, 2019, **19**, 2728–2740.

4 A. Schröder and E. Raphael, *Europhys. Lett.*, 1992, **17**, 565–570.

5 A. S. Dukhin and P. J. Goetz, *J. Chem. Phys.*, 2009, **130**, 124519.